JCI insight

Endothelial Response to Blood-Brain Barrier Disruption in the Human Brain

Andrew Gould, … , M. Luisa Iruela-Arispe, Adam M. Sonabend

JCI Insight. 2024. https://doi.org/10.1172/jci.insight.187328.

Resource and Technical Advance In-Press Preview **Neuroscience** **Vascular biology**

Cerebral endothelial cell (EC) injury and blood-brain barrier (BBB) permeability contribute to neuronal injury in acute neurological disease states. Preclinical experiments have used animal models to study this phenomenon, yet the response of human cerebral ECs to BBB disruption remains unclear. In our Phase 1 clinical trial (NCT04528680), we used low-intensity pulsed ultrasound with microbubbles (LIPU/MB) to induce transient BBB disruption of peri-tumoral brain in patients with recurrent glioblastoma. We found radiographic evidence that BBB integrity was mostly restored within 1-hour of this procedure. Using single-cell RNA sequencing and transmission electron microscopy, we analyzed the acute response of human brain ECs to ultrasound-mediated BBB disruption. Our analysis revealed distinct EC gene expression changes after LIPU/MB, particularly in genes related to neurovascular barrier function and structure, including changes to genes involved in the basement membrane, EC cytoskeleton, and junction complexes, as well as caveolar transcytosis and various solute transporters. Ultrastructural analysis showed that LIPU/MB led to a decrease in luminal caveolae, the emergence of cytoplasmic vacuoles, and the disruption of the basement membrane and tight junctions, among other things. These findings suggested that acute BBB disruption by LIPU/MB led to specific transcriptional and ultrastructural changes and could represent a conserved mechanism of BBB repair after neurovascular injury in humans.

Endothelial Response to Blood-Brain Barrier Disruption in the Human Brain

Andrew Gould[1,2], Yu Luan[3], Ye Hou[4], Farida V. Korobova[5], Li Chen[1,2], Victor A. Arrieta[1,2], Christina Amidei[1,2], Rachel Ward[1,2], Cristal Gomez[1,2], Brandyn Castro[1,2,6], Karl Habashy[1,2], Daniel Zhang[1,2,7], Mark Youngblood[1,2], Crismita Dmello[1,2], John Bebawy[1,8], Guillaume Bouchoux[9], Roger Stupp[1,2,10,11], Michael Canney[9], Feng Yue[2,3], M. Luisa Iruela Arispe[5], Adam M. Sonabend[1,2].*

[1]Department of Neurological Surgery, Feinberg School of Medicine, Northwestern University, Chicago, IL, USA
[2]Northwestern Medicine Malnati Brain Tumor Institute of the Lurie Comprehensive Cancer Center, Feinberg School of Medicine, Northwestern University, Chicago, IL, USA
[3]Department of Biochemistry and Molecular Genetics, Feinberg School of Medicine, Northwestern University, Chicago, IL, USA
[4]Institute of Biomedicine, College of Life Sciences, Inner Mongolia University, Hohhot, China
[5]Department of Cell and Developmental Biology, Feinberg School of Medicine, Northwestern University, Chicago, IL, USA
[6]Department of Neurosurgery, University of Chicago, Chicago, IL, USA
[7]Rush Medical College, Chicago, IL, USA
[8]Department of Anesthesiology, Feinberg School of Medicine, Northwestern University, Chicago, IL, USA
[9]Carthera, Lyon, France
[10]Department of Neurology, Feinberg School of Medicine, Northwestern University, Chicago, IL, USA
[11]Department of Medicine, Division of Hematology/Oncology, Feinberg School of Medicine, Northwestern University, Chicago, IL, USA

***** Correspondent author:

Adam M. Sonabend MD
adam.sonabend@northwestern.edu
Associate Professor of Neurological Surgery
Director of Translational Neuro-oncology
Department of Neurological Surgery
Feinberg School of Medicine
Northwestern University
676 N. St. Clair st
Suite 2210
Chicago IL
60611

Abstract:

Cerebral endothelial cell (EC) injury and blood-brain barrier (BBB) permeability contribute to neuronal injury in acute neurological disease states. Preclinical experiments have used animal models to study this phenomenon, yet the response of human cerebral ECs to BBB disruption remains unclear. In our Phase 1 clinical trial (NCT04528680), we used low-intensity pulsed ultrasound with microbubbles (LIPU/MB) to induce transient BBB disruption of peri-tumoral brain in patients with recurrent glioblastoma. We found radiographic evidence that BBB integrity was mostly restored within 1-hour of this procedure. Using single-cell RNA sequencing and transmission electron microscopy, we analyzed the acute response of human brain ECs to ultrasound-mediated BBB disruption. Our analysis revealed distinct EC gene expression changes after LIPU/MB, particularly in genes related to neurovascular barrier function and structure, including changes to genes involved in the basement membrane, EC cytoskeleton, and junction complexes, as well as caveolar transcytosis and various solute transporters. Ultrastructural analysis showed that LIPU/MB led to a decrease in luminal caveolae, the emergence of cytoplasmic vacuoles, and the disruption of the basement membrane and tight junctions, among other things. These findings suggested that acute BBB disruption by LIPU/MB led to specific transcriptional and ultrastructural changes and could represent a conserved mechanism of BBB repair after neurovascular injury in humans.

Introduction:

The blood-brain barrier (BBB) is a complex network of multiple cell types that lines the neurovasculature. It plays a crucial role in safeguarding the central nervous system (CNS) from harmful substances and maintaining an environment optimal for neuronal function (1, 2). The cerebral endothelial cells (ECs) are a key component of this barrier, forming a continuous layer that restricts transcellular and paracellular transport through specialized tight junction complexes, characteristic suppression of transcytosis, a dense basement membrane, and selective membrane transport proteins for essential nutrients and metabolites (3-6).

Cerebral ECs are integral to CNS homeostasis. Loss of barrier integrity has been implicated as a secondary mechanism of neuronal injury in acute neurological disease states, ranging from traumatic brain injury (TBI) to ischemic stroke (1, 2, 7-10). Animal studies have utilized electron microscopy to examine how sudden BBB disruption results in ultrastructural changes to ECs at the cerebral microvasculature, including the breakdown of TJs, increased transcytosis, and the breakdown of the basement membrane. These structural changes are a part of the “barrier breakdown” that results in pathological neurovascular permeability and contributes to the cerebral edema that serves as a secondary mechanism of neuronal injury in these disease states (11-14).

While this pathological permeability might be reversible, little is known about the process of barrier repair and return to BBB homeostasis in humans. Animal models have shown that acute BBB disruption induces cerebral ECs to alter transcription of genes related to intercellular adhesion, cytoskeletal organization, and attachment to the extracellular matrix. This implies that ECs are sensitive to barrier compromise and likely

play a role in the repair process that involves structural reorganization of their attachments to each other and the surrounding environment (15, 16). Studying how human cerebral ECs respond to acute BBB disruption could elucidate how barrier integrity is restored, CNS homeostasis is regained, and how to mitigate permanent neurological injury in these disease states.

The use of low-intensity pulsed ultrasound with microbubbles (LIPU/MB) has emerged as a technique to enhance the brain concentrations of systemically administered drugs for the treatment of tumors and other CNS diseases (17-23). In previous reports, including ours, LIPU/MB via a skull-implantable ultrasound array (the SonoCloud-9 or SC9, Carthera, Lyon, France) was used to induce temporary BBB disruption in patients with recurrent glioblastoma (GBM) (24, 25). This method has proven to be a safe, reproducible, and feasible as a means of enhancing concentrations of multiple drugs in the human brain (24, 26). Using contrast-enhanced magnetic resonance imaging (MRI), we showed that BBB opening within brain regions targeted by LIPU/MB (hereafter referred to as “sonication”) resolves rapidly, as permeability to gadolinium contrast was mostly reduced within an hour after this procedure (24, 25).

Having established the feasibility and kinetics of sonication-induced BBB opening, we leveraged LIPU/MB as a means of studying acute BBB disruption within the human brain in a controlled and consistent timeframe. Through our Phase I clinical trial NCT04528680, we used intraoperative sonication to induce transient BBB disruption in patients undergoing resection of recurrent GBM (24). After opening the BBB, we sampled non-eloquent sonicated peri-tumoral brain within minutes of the procedure (when the BBB was most permeable) and again at approximately 45 - 60 minutes afterwards, along with

non-sonicated control tissues. Using single-cell RNA sequencing (scRNA-seq) and transmission electron microscopy (TEM), we then studied the effects of ultrasound-mediated BBB disruption on the transcriptome and ultrastructure of microvascular ECs in the human brain.

Results:

Transcriptional Response of Human Cerebral Endothelium to Ultrasound-Mediated BBB Disruption

We used scRNA-seq to characterize the transcriptional response of human cerebral ECs to acute BBB disruption via sonication. As described previously, BBB disruption within sonicated peri-tumoral brain was mapped using fluorescein and fluorescence-based microsurgery (24). Fluorescein, which is typically restricted from crossing an intact BBB, accumulated in areas where the BBB was disrupted by LIPU/MB (22, 24). Thus, sonicated brain with increased BBB permeability exhibited notable fluorescence compared to adjacent non-sonicated brain not targeted by the ultrasound. A summary of the intraoperative LIPU/MB procedure and peri-tumoral biopsy process is shown in **Fig. 1.**

Each peri-tumoral brain sample was processed fresh into single cell suspensions and subjected to scRNA-seq library preparation (1 non-sonicated and 1 late sonicated peri-tumoral brain sample per patient, N = 6 patients, 12 brain samples in total). Unsupervised analysis led to 14 distinct gene expression-based cell clusters, that were designated as either oligodendrocytes, microglia, T-cells, ECs, monocytes, pericytes, oligodendroglial-progenitor cells, natural killer cells, B-cells, or glioma/astrocytes. We focused our analysis on ECs given their vital role in barrier function at the neurovasculature. We analyzed 2643 ECs, including 1470 from sonicated and 1173 derived from non-sonicated peri-tumoral brain specimens (**Fig. 2A).** A Uniform Manifold Approximation and Projection (UMAP) plot of these ECs was generated with cell labeling

done according to whether these derived from late sonicated or non-sonicated control samples (**Fig. 2B**).

Gene-set enrichment analysis (GSEA) of EC transcriptomics revealed significant alterations in gene transcription following sonication, impacting several ontology themes of interest in the context of the BBB (adjusted P <0.05). Notably, there was downregulation of Gene Ontology (GO) themes Regulation of Endocytosis (normalized enrichment score NES=-2.01), Blood Vessel Morphogenesis (NES=-2.08), Cell Matrix Adhesion (NES=-2.13), Abnormality of Cerebral Vasculature (NES=-2.01), Structural Component of Cytoskeleton (NES=-1.96) and Cell-Cell Adhesion (NES=-2.04). Conversely, there was an upregulation of the theme Active Transmembrane Transporter activity (NES=2.23) (**Fig. 2C)**. The heatmap in **Fig. 3** shows the expression changes of individual genes within these GO themes, comparing sonicated and non-sonicated brain ECs. Notable changes included altered transcription of genes previously implicated in neurovascular biology and barrier function. This included the downregulation of *GPR4* (log2FC= -0.3748953, adjusted P = 1.08E-18), a pH-sensing G-protein-coupled receptor in cerebral ECs that modulates cAMP signaling and is crucial for cerebrovascular integrity (27, 28). Other alterations were observed in genes associated with selective transcytosis across the BBB. For example, we observed downregulation of transcripts for the gene of the Low-density-lipoprotein receptor (*LDLR*), expressed in cerebral ECs and used to mediate transcytosis (log2FC = -0.29, adjusted P = 1.61E-09) (29, 30). Notably, sonication was also associated with significantly altered expression of various genes within the Solute Carrier (SLC) and Organic Ion (SLCO) superfamilies of membrane transport proteins. These transporters have been previously associated with influx and

efflux of various substances across the neurovasculature and maintain a cerebral spinal fluid (CSF) ionic milieu that is conducive to proper neuronal development and function (31). Notable expression changes within these families included upregulation of genes: *SLC38A3* (log2FC = 0.74, adjusted P = 1.14E-28) and *SLC38A5* (log2FC = 0.28, adjusted P = 3.34E-4), both coding for transporters specific for nitrogen-rich amino acids that can remove excess glutamine/glutamate from the CSF to the endothelium, likely as a means of avoiding excitotoxicity (31, 32); *SLC7A5* (log2FC = 0.76, adjusted P = 9.47E-44), a transporter of various neutral amino acids that also plays a role in glutamine/glutamate homeostasis in the CSF (31, 33); downregulation of *SLC4A7* (log2FC = -0.331, adjusted P = 4.78E-11), a sodium/bicarbonate cotransporter responsible for maintaining appropriate ionic concentrations and pH in the CSF (34); and simultaneous upregulation of *SLCO1A2* (log2FC = 0.553, adjusted P = 4.25E-15) and *SLCO4A1* (log2FC = -0.313, adjusted P = 2.64E-14), both sodium independent uptake transporters thought to play a role in drug delivery across the neurovasculature (35-37).

BBB Disruption Alters Endothelial Cell and Basement Membrane Morphology in Brain Capillaries

Previous animal studies employed TEM to examine the effects of sonication on the ultrastructure of the cerebral microvasculature and ECs. These studies highlighted structural changes associated with acute BBB disruption, including irregular “opening” of the TJs between ECs that could facilitate paracellular drug delivery following sonication (38, 39). Therefore, we used TEM to study the ultrastructural changes induced by sonication to cerebral ECs in human peri-tumoral brain specimens. For this, we acquired

peri-tumoral brain specimens from early sonicated (within 15 minutes of LIPU/MB), late sonicated (at least 45 minutes after LIPU/MB), and non-sonicated peri-tumoral brain biopsies (at least 45 minutes after LIPU/MB) from three separate patients (N = 9 tissue biopsies, 3 per patient). Using TEM, we then imaged capillary cross-sections from each tissue specimen (non-sonicated N = 17, early sonicated N = 18, late sonicated N = 21) from each patient.

These electron micrographs were analyzed by L.A., an expert in cell biology and vascular pathology, who conducted a blinded review of the images. The expert was able to identify vessels as sonicated (either timepoint) and non-sonicated with 100% accuracy. A spectrum of key morphological distinctions was noted and used to distinguish between sonicated and non-sonicated vessels. First, it was observed that the basement membrane of sonicated capillaries frequently displayed granular or amorphous deposits that disrupted its continuity (**Fig. 4A**). Second, sonicated ECs often showed evidence of cytosol rarefaction and disorganization of the cytoskeleton (**Fig. 4B**). TJ complexes of sonicated ECs occasionally appeared less “dense” than their non-sonicated counterparts, sometimes with irregular spaces and “opening” of the intercellular cleft (**Fig. 4C**). In line with these observations, our scRNA-seq analysis revealed that sonication was associated with changes in the transcription of genes coding for structural components of the basement membrane, and TJ/adherens junction complex. Notable changes included the downregulation of *COL4A1* coding for collagen type IV alpha 1 chain (log2FC = -0.34, adjusted P = 7.9E-10), an essential component of the endothelial basement membrane linked to BBB integrity. In line with this, mutations in this gene have been implicated in intracerebral hemorrhage in mice (40, 41). We also noted downregulation of *CDH5*, which

codes for cadherin-5 (log2FC = -0.288, adjusted P = 3E-7), a major component of the adherens junctions found between cerebral ECs (1, 42). Conversely, there was upregulation of *CGNL1* which codes for paracingulin, a protein localized to the cytoplasmic region of the apical portion of the TJ/adherens complex of brain ECs (log2FC = 0.457, adjusted P = 8.2E-3) (6, 43, 44). We also observed downregulation of *ACTB* coding for actin beta (log 2FC = -0.86, adjusted P = -2.8E-6), a cytoskeletal protein whose remodeling has been implicated in reorganization of the endothelial TJs under periods of BBB permeability following mechanical stimuli and ischemic injury to the endothelium **(Fig. 4D)** (5, 45). In sum, the combined results from our TEM and scRNA-seq analyses indicate that LIPU/MB-induced BBB disruption is associated with marked changes to the morphology and transcriptional activity of human cerebral ECs that could be related to increased neurovascular permeability. These changes appear to exert a particularly strong effect on intercellular junctions, the basement membrane, and cytoskeleton.

Ultrasound-Mediated BBB Disruption Alters Cerebral Endothelial Caveolar Pit Density in a Time-Dependent Fashion

Building on previous animal studies which suggested that enhanced caveolar transcytosis in sonicated capillaries acted as a secondary mechanism of drug delivery across the BBB following sonication (39), we aimed to assess the density of endothelial caveolae in sonicated and non-sonicated peritumoral brain tissues. Since we previously found that peak BBB permeability after sonication occurred within 15 minutes of LIPU/MB (24), and barrier integrity returned quickly thereafter (**Fig. 5A, B, C**), we collected peri-tumoral brain specimens within this 15 minute window of maximum permeability. We

counted well-formed caveolar pits (approx. 40 – 80 nm in diameter) that were attached to the basal and luminal membranes of the ECs (**Fig. 6A)**. Using a linear mixed-effects model, we noted a significant effect of sonication on the frequency of luminal caveolar pits (Chi-square, P = 0.01542). Post-hoc analysis showed decreased numbers of luminal caveolae in the peri-tumoral brain collected at the early sonicated timepoint compared to the non-sonicated timepoint (Chi-square, P = 0.0185). Non-statistically significant trends were found for numbers of luminal caveolae between late sonicated and non-sonicated ECs (Chi-square, P = 0.0734). According to the same mixed-effects model, sonication did not have an effect on the frequency of basal caveolae (Chi-square, P = 0.1049; **Fig. 6B**). Post-hoc analysis also showed no significant relationship between the frequency of basal caveolae counted in capillary cross-sections, when comparing non-sonicated to early sonicated (Chi-square, P = 0.0983), non-sonicated to late sonicated (Chi-square, P = 0.3794), or early to late sonicated timepoints (Chi-square, P = 0.6751).

In line with these observations, our GSEA analysis highlighted a downregulation in the GO theme Regulation of Endocytosis in sonicated ECs, as previously mentioned (normalized enrichment score NES=-2.01, adjusted P = 0.0432) **(Fig. 6C).** We also noted that sonication altered the transcription of genes related to caveolar transcytosis, including increased expression of *MFSD2A* (log2FC = 0.592, adjusted P = 1.31E-36) and decreased expression of *CAV1* (average log2 fold-change in expression for sonicated ECs over non-sonicated cells, log2FC = -0.77, adjusted P = 1.14E-32) **(Fig. 6D)**. *MFSD2A* codes for a lysophosphatidylcholine symporter that has previously been characterized as essential to maintaining BBB function and repressing caveolar transcytosis at the cerebral endothelium, while *CAV1* codes for a protein component of caveolae (3, 4). Moreover,

281 selective enrichment of Mfsd2a in rats was shown to attenuate caveolar transcytosis, BBB
282 permeability, and neuronal injury in the days following experimentally induced sub-
283 arachnoid hemorrhage (46, 47). Therefore, our TEM and transcriptional analyses could
284 suggest that, within the one-hour timeframe we explored after BBB disruption, caveolar
285 transcytosis does not appear to be enhanced in human cerebral ECs.

286
287 **BBB disruption by LIPU/MB leads to cytoplasmic vacuoles in endothelial cells.**

288 Upon further examination of our electron micrographs, we observed that sonicated
289 ECs demonstrated large cytoplasmic vacuoles more frequently than non-sonicated ECs.
290 These structures varied greatly in size but were much larger than and distinct from the
291 membrane-bound caveolae noted previously (**Fig. 7A**). To determine if these vacuoles
292 were more frequent in sonicated blood vessels and to explore any time-dependent
293 relationship to their frequency, we quantified their numbers in the EC cytoplasm. We then
294 normalized these counts to the cross-sectional surface area of the EC cytoplasm in the
295 micrograph for each vessel. Using a linear mixed-effects model, we found that sonication
296 had a significant effect on the frequency of these vacuoles (Chi-square, $P = 0.004282$;
297 **Fig. 7B**). The post-hoc analysis highlighted a significant difference specifically between
298 the late sonicated and non-sonicated groups ($P = 0.0036$). However, no significant
299 differences were found for early sonicated and late sonicated groups ($P = 0.3379$), or the
300 early sonicated and non-sonicated groups ($P = 0.1313$). These findings indicate that
301 LIPU/MB-mediated BBB disruption leads to notable morphological changes within ECs,
302 particularly in the formation of cytoplasmic vacuoles, that tend to increase over time.

Discussion:

Here we have leveraged scRNA-seq and TEM to characterize the transcriptional response and ultrastructural changes to human cerebral ECs in an acute state of BBB disruption following LIPU/MB. Our study provides human data on the processes related to BBB disruption and restoration shortly after insult. A summary of some of the key structural and transcriptional changes is illustrated in **Fig. 8.**

Previous studies characterized the transcriptome of the human ECs in health and vascular pathology (48-50). Yet, to our knowledge, transcriptional and structural changes in response to acute BBB disruption have only been studied in animal models. Many of the gene expression changes we identified, such as *CDH5* and *COL4A1*, encode proteins that have previously been identified as structural components of the neurovascular unit and BBB, which impede passive diffusion of substances from the blood into the brain. Abnormal organization or absence of these components have been implicated in enhanced BBB permeability (40, 42). Other genes, such as *MFSD2A, CAV1, LDLR,* and *SLC/SLCO* family transporters, have previously been implicated in regulating transcytosis or allowing for selective delivery of substances across the BBB (3, 4, 30, 31).

Our GO analysis also revealed that sonication induced significant changes to themes related to intercellular and cell-matrix adhesion, cytoskeletal organization, and vascular morphogenesis. Given that the established mechanism of LIPU/MB-enhanced drug delivery involves mechanical separation of ECs, these transcriptional changes could reflect a transient suppression of EC genes coding for components of the neurovascular ultrastructure, as suggested by our TEM analyses, wherein sonicated capillaries showed occasional disassembly of tight junctions, rarefaction of EC cytosol, and

amorphous/granular deposits in the basement membrane that might reflect mechanical perturbation of the microvasculature. Some of these TEM findings had also been described in other preclinical models of BBB disruption, including LIPU/MB, ischemic stroke, and TBI (11, 14, 38, 51).

Using TEM, we observed a significant increase in the frequency of cytoplasmic vacuoles in sonicated ECs, which to our knowledge, had not been described previously. Their functional relevance remains unknown. Prior *in vitro* studies utilizing scanning electron microscopy had noted that alternating acoustic pressures of ultrasound, with or without microbubbles, could form pores in cell membranes that render cells more permeable to drug delivery (52). The vacuoles we identified on TEM could be cross sections of these pores channeling through ECs, or alternatively, they could play some role in the pinocytosis of substances across the neurovasculature. However, we found these structures to be most frequent at a time point after sonication when we observed permeability to gadolinium to already be greatly diminished (24). As permeability to gadolinium might differ to that of other substances, the potential contribution of these vacuoles to drug transport across the BBB remains to be determined.

With regards to transcytosis, our transcriptional analysis showed that sonication altered expression of various genes previously implicated in EC transporter activity and the regulation of endocytosis. This included increased expression of various *SLC/SLCO* family genes that are established regulators for concentrations of various metabolic substrates and ions in the brain interstitial space (31-37). it is possible that the increased expression of these transporters reflects a compensatory mechanism to correct abnormal

concentrations of various amino acids and ions that could accumulate in the brain following sonication.

Contrary to preclinical TEM studies of LIPU/MB (38, 39), we did not find a time-dependent increase in the frequency of EC caveolae within an hour of sonication. However, we observed a time-dependent decrease in the frequency of luminal caveolar pits 4-15 minutes after sonication, a timepoint not explored by earlier studies (38). This discrepancy could have resulted from a difference in timing of tissue acquisition after sonication. Another possible explanation for this is that, while prior studies reported an increase in the number of EC caveolae, this effect was only statistically significant in arterioles (39). Given that our tissue biopsies were taken from the superficial cortex, most blood vessels we identified were capillaries with rare arterioles and venules. Thus, we restricted our analysis to capillaries and were unable to consider consequences of LIPU/MB on caveolar transcytosis at non-capillary components of the cerebral microvasculature. Another possibility could be that, in human cerebral ECs, caveolae don't play a substantial role in transcytosis following LIPU/MB. This is suggested by the increased transcription of the gene *MFSD2A,* which is known to inhibit caveolae-mediated transcytosis, as well as decreased transcription of *CAV1* that we noted in sonicated ECs. It has also been reported that caveolae have alternative functions unrelated to transcytosis, particularly at the neurovasculature. Prior electron microscopic studies performed *in vitro* reported that caveolae can "flatten" in response to mechanical forces such as uniaxial stretching. In this sense, they act as membrane redundance or a "reservoir" that buffers mechanical stresses across the cell and protects it from rupturing (53). Moreover, integrin detachment and altered cell adhesion can cause caveolar pits to

rapidly flatten and their density to decrease and then normalize within minutes upon re-adhesion (54). Consistent with this, we only encountered a decrease in caveolae in the luminal membrane of sonicated ECs, which are more likely to be directly targeted by the pressure of microbubble cavitation. Given that LIPU/MB is thought to mechanically separate adjacent ECs, the initial decrease in membrane-bound caveolae we observed immediately after sonication might reflect EC detachment from their intercellular connections and the underlying basal lamina. In line with this, normalization of the caveolar pit density within an hour of sonication coincided with partial restoration of BBB integrity (as also evidenced by our radiographic studies). Thus, our TEM analysis suggests that the immediate decrease in the frequency of caveolae could contribute to cellular resilience to mechanical stress, and BBB homeostasis following microbubble cavitation, while enhanced caveolar transcytosis may not contribute to increased permeability in human cerebral capillary ECs in a state of BBB disruption, at least within one hour of LIPU/MB.

Our study assessed the response of cerebral ECs to BBB disruption at a very acute timepoint (within an hour of sonication). We chose this timepoint for logistical reasons pertaining to chemotherapy infusion during the surgery, but it also coincided with our previous estimates on the kinetics of BBB and restoration of barrier function to gadolinium (24). Imaging studies in patients undergoing transcranial focused ultrasound (FUS) have reported variable timelines on the return of barrier function. Some estimate persistent BBB permeability 2 to 6 hours after LIPU/MB, while others put it at 24 hours (21, 25, 55-57). This variability could be accounted for by differences in the acoustic parameters and the modality of ultrasound used to open the BBB in each study (transcranial versus skull-

implantable). Our study utilized a mechanical index of 1.03 MPa. This parameter was decided upon after previous clinical trials found it to be optimal for safe and effective BBB disruption using the SC9, where sound waves do not penetrate across bone (18, 56). In a recent publication by Carpentier et al., wherein patients with recurrent GBM underwent serial sonication-enhanced chemotherapy with the SC9, they reported hypointense lesions in SWI sequences seen on MRI suggestive of microhemorrhages in 6 out of 52 sonications (11%) (25).

While we focused on the response of the ECs to LIPU/MB, it's possible that the transcriptional and structural changes we report are not unique to LIPU/MB-based BBB disruption. Munji et al., examined the transcriptional alterations within the cerebral ECs of rodents in various experimental models of acute BBB disruption, including TBI, ischemic stroke, seizure, and autoimmune encephalomyelitis (15). Distinct transcriptional alterations were noted for each model, but there was also a core module of 54 genes whose transcripts were consistently enriched across all models at the time of peak BBB disruption. The authors speculated that this core module could reflect a conserved mechanism of regulating EC permeability and BBB repair (15). Some of these alterations were found on GO themes similar to those of our analysis, including cell adhesion ECM-receptor interaction, and regulation of angiogenesis.

In conclusion, we characterized the transcriptional and ultrastructural alterations of LIPU/MB-mediated BBB disruption on human cerebral ECs at an acute timepoint. For this we relied on intraoperative LIPU/MB of peri-tumoral brain to model this process in human cerebral tissues. We show that loss of BBB integrity is associated with altered expression of genes that relate to EC structure, attachment, and transcytosis. We also

show that sonication alters the physical phenotype of ECs and the broader neurovascular ultrastructure. While our findings highlight acute changes seen after sonication, they present some similarity to EC changes reported in acute neurological disease states where permeability of the BBB has been implicated, thus our data might provide insight into mechanisms of BBB homeostasis and EC response to microvascular injury in the human brain seen in various neurological pathologies. Work should also be done to further characterize changes to cerebral ECs at later timepoints than what we were able to explore. Though this presents obvious logistical hurdles, exploring the mechanisms of neurovascular permeability and recovery in the late stages of these diseases could reveal valuable targets for molecular therapies that may be used in the acute setting to attenuate permanent neuronal injury secondary to pathological BBB permeability.

Methodology:

Sex as a Biological Variable:

Sex was not considered as a biological variable for the purposes of this study, due to availability of tissue samples and focus of the disease. Tissues for this study were acquired from both male and female participants. The sex of each study participant from whom tissue biopsies are reported in supplementary table 1.

Intraoperative LIPU/MB-Enhanced Chemotherapy and Stereotactic Biopsy of Sonicated Peri-tumoral Brain:

Enrolled patients received treatment as described previously (24). In brief: The use of intraoperative corticosteroids or mannitol was avoided for all cases where we performed intraoperative pharmacokinetic studies. Biopsy of non-eloquent peri-tumoral brain was performed when feasible and justified as per standard neurosurgical technique. For these studies we decreased the FiO2 as much as tolerated up to 20% aiming to obtain an arterial O2 pressure <100 mm/Hg, to model the outpatient setting where patients are on room air. We exposed the peri-tumoral brain to be excised, positioned the SC9 device in the cranial window, flooded the field with sterile saline, connected the device to the SC9 radiofrequency generator, and infused intravenous (IV) DEFINITY 10 μL/kg (Lantheus) microbubbles while sonicating the brain for a duration of 270 seconds using an acoustic pressure of 1.03 MPa, as was used in our recent clinical trials with the SonoCloud-9 System(24, 25). Immediately after sonication, we infused fluorescein 500 mg IV, and initiated a 45 minute IV infusion of nab-paclitaxel chemotherapy (Abraxane). LIPU/MB-based BBB opening was visualized and mapped using fluorescent microscopy

(ZeissTM Yellow 560 nm filter). Sonicated peri-tumoral brain was identified by fluorescent microscopy following infusion of fluorescein and non-sonicated peri-tumoral brain based on absence of fluorescence in this setting. Within 4-15 minutes of sonication (referred to as early timepoint), we obtained biopsies of ineloquent sonicated peri-tumoral brain where feasible, which were immediately fixed for TEM. Following the remainder of the 45-minute infusion period, we further biopsied paired sonicated and non-sonicated ineloquent peri-tumoral brain for additional TEM analysis and scRNA-seq. Samples intended for sequencing were transported in saline on ice and underwent immediate processing. Representative fluorescent photographs of the brain, and corresponding stereotaxic coordinates were obtained for each biopsy. This was followed by standard tumor resection, and permanent implantation of the SC9 at the end of the procedure.

Single-cell RNA sequencing:

Patients whose tissues were used for scRNA-seq analysis did not receive dexamethasone prior to obtaining these biopsies. RNA sequencing was performed for paired sonicated and non-sonicated peri-tumoral brain specimens collected at approximately 45 minutes after LIPU/MB per patient. Peri-tumoral brain was defined as brain parenchyma that was not enhancing per the contrast MRI used for stereotaxic navigation. Sonicated brain was identified by fluorescent microscopy following infusion of fluorescein and non-sonicated brain based on absence of fluorescence in this setting. Each tissue sample was processed fresh into single cell suspensions and subjected to scRNA-seq library preparation. Samples were transported on ice, and single-cell suspension was performed using the Miltenyi Biotec system on gentleMACS™ Octo

Dissociator (Miltenyi Biotec) according to the manufacturer's instructions. Isolated cells were washed with PBS containing 0.04% bovine serum albumin and filtered through a 40-µm cell strainer. Cell concentration and viability were determined by a Countess II Automated Cell Counter with a final cell concentration of 700-1,200 cells/ul. scRNA-seq libraries were generated using the Chromium Single Cell 3′ Reagent Kit (10X Genomics). Single-cell suspension was mixed with RT-PCR master mix and loaded together with Single Cell 3′ Gel Beads and Partitioning Oil into a Single Cell 3′ Chip (10X Genomics). The cDNA was amplified and further used to construct 3' gene expression library according to the manufacturer's instructions. The size profiles of pre-amplified cDNA and sequencing libraries were examined by the Agilent High Sensitivity 2100 Systems (Agilent). The scRNA-seq library was sequenced on the Illumina NextSeq 500/550 platform.

Single-cell transcriptomic analysis:

All the scRNA-seq data were aligned to GRCh38 reference genome and quantified using Cell Ranger pipeline (https://support.10xgenomics.com/single-cell-gene-expression/software/pipelines/latest/what-is-cell-ranger) by running cellranger count, we kept the filtered data from Cell Ranger for the further quality control.

Doublet Removal and QC: The filtered_feature_bc_matrix generated by Cell Ranger pipeline was processed with Seurat (58). Cells with fewer than 200 unique genes or greater than 4000 genes were removed. The remaining cells in each sample were used as the input of DoubletFinder (59). The first 20 PCs with the pN=0.25 and pK=0.09 were used to identify the doublets. The cells that were classified as doublets were then

503 removed. The remaining cells from 12 samples were merged as a single Seurat object.
504 To further remove the dead or dying cells, we filtered the cells by percentage of
505 mitochondrial reads per cell greater than 15% or with greater than 20,000 counts.
506 Batch Effect Removal, Dimensionality Reduction, Clustering and Cell Annotation: Cells
507 from the Seurat object were analyzed with standard workflow of Seurat. First,
508 NormalizeData was run using the LogNormalize method and the scale factor with 10,000
509 for cell level normalization. The variable features were identified by findVariableFeatures
510 using vst method with 2,000 features. The data was scaled to 10,000 UMIs per cell and
511 PCs were computed with RunPCA. The batch effect correction was performed using
512 Harmony (60). UMAP was generated from the results of batch corrected PCs. The cells
513 were then clustered using FindNeighbors with batch corrected first 20 dimensions, and
514 FindClusters with a resolution of 0.5. Briefly, we determined the k-nearest neighbors of
515 each cell and use KNN graphs to construct the SNN graph by calculating the
516 neighborhood overlap (Jaccard index) between every cell and its k.param nearest
517 neighbors to determine the unsupervised cell clusters. Cluster specific marker genes
518 were defined by Wilcoxon test with padj < 0.01 and avg_logFC > 0.5. Clusters were
519 annotated to cell types by comparing marker genes for each cluster to cell type markers
520 from Panglaodb marker gene database (61) corresponding to expected human brain cell
521 types. For example, *P2RY12*, *PTGS1* were used to define Microglia cells, *CNP* and *PLP1*
522 were used to define Oligo cells, *FTL1*, *LYZ*, *IL7R* were used to define Endothelial,
523 Monocyte, and T-Cell, respectively (48, 62-65).
524 Differential expression and functional enrichment analysis: We performed differential
525 expression analysis between sonicated and non-sonicated samples across each cell type

using Wilcoxon test and Benjamini-Hochberg method was used to estimate the false discovery rate (FDR), and following the recommendation of Seurat. The DEGs were filtered using avg_logFC > 0.5 and padj < 0.05. The functional enrichment analysis for DEGs between sonicated and non-sonicated sample was conducted using clusterProfiler R package (66).

Electron microscopy analysis:

Patients whose tissues were used for ultrastructural analysis of peri-tumoral brain by TEM did not receive dexamethasone prior to obtaining the biopsies. For electron microscopy, approximately 1-2 mm^3 samples of brain tissue subject to LIPU/MB or not, were excised and fixed in a mixture of 2.5% glutaraldehyde and 2% paraformaldehyde in 0.1M cacodylate buffer for 2 or 3 hours or overnight in 4°C. Post-fixation, tissue was exposed to 1% osmium tetroxide and 3% uranyl acetate, dehydrated in ethanol, embedded in Epon resin and polymerized for 48 hours at 60 C. Then ultra-thin sections were made using Ultracut UC7 Ultramicrotome (Leica Microsystems) and contrasted with 3% uranyl acetate and Reynolds's lead citrate. Samples were imaged using a FEI Tecnai Spirit G2 transmission electron microscope (FEI Company, Hillsboro, OR) operated at 80 kV. Images were captured by Eagle 4k HR 200kV CCD camera.

Caveolar pits were identified as membrane-bound invaginations (40-80 nm in diameter) that were directly attached to the basal and luminal surfaces of endothelial cells. Caveolae were also distinguished from clathrin-coated vesicles according to their size, as well as by the density and absence of obvious protein spike along their membrane surfaces. Only well-formed caveolae, showing direct attachment to either of the

endothelial membranes were counted for this analysis. Cytoplasmic vacuoles were identified as single membrane vesicles ranging in sizes (150—250 nm in diameter) without any electron-dense content in majority cases.

Statistical Analysis of Transmission Electron Micrographs:

We utilized a mixed-effects linear model to assess the effect of sonication status on the frequency of basal and luminal endothelial caveolae and vacuoles relative to the cross-sectional surface area of the endothelial cytoplasm. For each type of cellular structure, models were constructed to compare a null scenario, considering inter-patient variability, with an alternative model that included sonication status as a fixed effect. *P* values were obtained by likelihood ratio tests of the full model with the effect in question against the model without the effect in question. Post-hoc analyses were also used to determine any relationship between the frequency of these structures at non-sonicated, early sonicated, and late sonicated timepoints.

Study Approval:

This study was approved by the institutional review board of Northwestern University Feinberg School of Medicine (STU00212298), and all patients provided written informed consent, which included consent for the translational pharmacokinetic study and for nonidentifiable data collected to be included in scientific publications. Quality assurance monitors from the Clinical Trials Office at the Robert H Lurie Comprehensive Cancer Center of Northwestern University verified the underlying study data and confirmed the accuracy of the results presented in this article.

Data Availability:

The scRNA-seq data have been deposited to the NCBI's Gene Expression Omnibus (GSE208074). Supporting data values for all figures and analyses can be found in the Supporting Data Values file, which can be found in the online supplemental material.

Author contributions:

Single-cell suspension was performed by LC, CD, VAA and BC. scRNA-seq analysis was performed by YL, YH and MY under the supervision of FY. Electron microscopy and related analyses were performed by FVK, AG, DZ, and MLIA. CA, RW, CG, JB, RS, AMS managed the clinical and regulatory aspects of the clinical trial for the correlatives presented. GB and MC performed the imaging analysis and sonication-related technical assistance. Manuscript was drafted by AG, KH, VAA and AMS. Statistical analysis was performed by VAA. Surgery and intraoperative LIPU/MB was performed by AMS with assistance from CA, CG, RW, AG and JB. AMS designed and supervised the project.

Acknowledgments:

This work was supported by the NIH grant 1R01NS110703-01A1 (AMS), NIH/NCI 1U19CA264338-01 (A.M.S. and R.S.), NIH/NCI 1R01CA245969-01A1 (A.M.S. and R.S,), P50CA221747 SPORE for Translational Approaches to Brain Cancer. Additionally, this work was supported by generous philanthropic support from the Moceri Family Foundation, Tina and Victor Kedaitis, as well as Emily and John Kos. Imaging work was performed at the Northwestern University Center for Advanced Microscopy (RRID:

SCR_020996) generously supported by NCI CCSG P30 CA060553 awarded to the Robert H Lurie Comprehensive Cancer Center.

Competing interests:

AMS and RS have received in-kind and or funding support for research from Agenus, BMS, and Carthera. AMS, VAA, CA, RS and DZ are co-authors of IP filed by Northwestern University related to LIPU/MB. AMS has served as a paid consultant for Carthera, EnClear Therapies, and Alpheus Medical. RS has acted or is acting as a scientific advisor or has served on advisory boards for the following companies: Alpheus Medical, AstraZeneca, Boston Scientific, Carthera, Celularity, GT Medical, Insightec, Lockwood (BlackDiamond), Northwest Biotherapeutics, Novocure, Inc., Syneos Health (Boston Biomedical), TriAct Therapeutics, Varian Medical Systems. GB and MC are employees and hold ownership interest in Carthera. JB is a paid consultant of Surveyor Biosciences Inc. MC and GB have patents related to the ultrasound technology described herein. RS is an advisory member and consultant for Carthera. All other authors declare that they have no competing interests.

References:

1. Profaci CP, Munji RN, Pulido RS, and Daneman R. The blood-brain barrier in health and disease: Important unanswered questions. *J Exp Med.* 2020;217(4).
2. Sweeney MD, Zhao Z, Montagne A, Nelson AR, and Zlokovic BV. Blood-Brain Barrier: From Physiology to Disease and Back. *Physiol Rev.* 2019;99(1):21-78.
3. Andreone BJ, Chow BW, Tata A, Lacoste B, Ben-Zvi A, Bullock K, et al. Blood-Brain Barrier Permeability Is Regulated by Lipid Transport-Dependent Suppression of Caveolae-Mediated Transcytosis. *Neuron.* 2017;94(3):581-94.e5.
4. Ben-Zvi A, Lacoste B, Kur E, Andreone BJ, Mayshar Y, Yan H, et al. Mfsd2a is critical for the formation and function of the blood-brain barrier. *Nature.* 2014;509(7501):507-11.
5. Luissint A-C, Artus C, Glacial F, Ganeshamoorthy K, and Couraud P-O. Tight junctions at the blood brain barrier: physiological architecture and disease-associated dysregulation. *Fluids and Barriers of the CNS.* 2012;9(1):23.
6. Stamatovic SM, Johnson AM, Keep RF, and Andjelkovic AV. Junctional proteins of the blood-brain barrier: New insights into function and dysfunction. *Tissue Barriers.* 2016;4(1):e1154641.
7. Krueger M, Härtig W, Frydrychowicz C, Mueller WC, Reichenbach A, Bechmann I, et al. Stroke-induced blood-brain barrier breakdown along the vascular tree - No preferential affection of arteries in different animal models and in humans. *J Cereb Blood Flow Metab.* 2017;37(7):2539-54.
8. Johnson VE, Weber MT, Xiao R, Cullen DK, Meaney DF, Stewart W, et al. Mechanical disruption of the blood-brain barrier following experimental concussion. *Acta Neuropathol.* 2018;135(5):711-26.
9. Cash A, and Theus MH. Mechanisms of Blood-Brain Barrier Dysfunction in Traumatic Brain Injury. *Int J Mol Sci.* 2020;21(9).
10. Leaston J, Qiao J, Harding IC, Kulkarni P, Gharagouzloo C, Ebong E, et al. Quantitative Imaging of Blood-Brain Barrier Permeability Following Repetitive Mild Head Impacts. *Front Neurol.* 2021;12:729464.
11. Knowland D, Arac A, Sekiguchi KJ, Hsu M, Lutz SE, Perrino J, et al. Stepwise recruitment of transcellular and paracellular pathways underlies blood-brain barrier breakdown in stroke. *Neuron.* 2014;82(3):603-17.
12. Nahirney PC, Reeson P, and Brown CE. Ultrastructural analysis of blood-brain barrier breakdown in the peri-infarct zone in young adult and aged mice. *J Cereb Blood Flow Metab.* 2016;36(2):413-25.
13. Thomsen MS, Routhe LJ, and Moos T. The vascular basement membrane in the healthy and pathological brain. *J Cereb Blood Flow Metab.* 2017;37(10):3300-17.
14. Krueger M, Bechmann I, Immig K, Reichenbach A, Härtig W, and Michalski D. Blood-brain barrier breakdown involves four distinct stages of vascular damage in various models of experimental focal cerebral ischemia. *J Cereb Blood Flow Metab.* 2015;35(2):292-303.
15. Munji RN, Soung AL, Weiner GA, Sohet F, Semple BD, Trivedi A, et al. Profiling the mouse brain endothelial transcriptome in health and disease models reveals a core blood-brain barrier dysfunction module. *Nat Neurosci.* 2019;22(11):1892-902.

16. Garcia-Bonilla L, Shahanoor Z, Sciortino R, Nazarzoda O, Racchumi G, Iadecola C, et al. Brain and blood single-cell transcriptomics in acute and subacute phases after experimental stroke. *bioRxiv.* 2023.
17. Bae S, Liu K, Pouliopoulos AN, Ji R, Jiménez-Gambín S, Yousefian O, et al. Transcranial Blood-Brain Barrier Opening in Alzheimer's Disease Patients Using A Portable Focused Ultrasound System with Real-Time 2-D Cavitation Mapping. *medRxiv.* 2024.
18. Carpentier A, Canney M, Vignot A, Reina V, Beccaria K, Horodyckid C, et al. Clinical trial of blood-brain barrier disruption by pulsed ultrasound. *Sci Transl Med.* 2016;8(343):343re2.
19. Drean A, Lemaire N, Bouchoux G, Goldwirt L, Canney M, Goli L, et al. Temporary blood-brain barrier disruption by low intensity pulsed ultrasound increases carboplatin delivery and efficacy in preclinical models of glioblastoma. *J Neurooncol.* 2019;144(1):33-41.
20. Gould A, Arrieta Gonzales VA, Dmello CC, Saganty R, Lukas RV, Zhang DY, et al. Advances in Blood-Brain Barrier Disruption to Facilitate Drug Delivery for Infiltrative Gliomas. *Advances in Oncology.* 2023;3(1):77-86.
21. Mainprize T, Lipsman N, Huang Y, Meng Y, Bethune A, Ironside S, et al. Blood-Brain Barrier Opening in Primary Brain Tumors with Non-invasive MR-Guided Focused Ultrasound: A Clinical Safety and Feasibility Study. *Sci Rep.* 2019;9(1):321.
22. Zhang DY, Dmello C, Chen L, Arrieta VA, Gonzalez-Buendia E, Kane JR, et al. Ultrasound-mediated Delivery of Paclitaxel for Glioma: A Comparative Study of Distribution, Toxicity, and Efficacy of Albumin-bound Versus Cremophor Formulations. *Clin Cancer Res.* 2020;26(2):477-86.
23. Kim KS, Habashy K, Gould A, Zhao J, Najem H, Amidei C, et al. Fc-enhanced anti-CTLA-4, anti-PD-1, doxorubicin, and ultrasound-mediated blood-brain barrier opening: A novel combinatorial immunotherapy regimen for gliomas. *Neuro Oncol.* 2024;26(11):2044-60.
24. Sonabend AM, Gould A, Amidei C, Ward R, Schmidt KA, Zhang DY, et al. Repeated blood-brain barrier opening with an implantable ultrasound device for delivery of albumin-bound paclitaxel in patients with recurrent glioblastoma: a phase 1 trial. *Lancet Oncol.* 2023;24(5):509-22.
25. Carpentier A, Stupp R, Sonabend AM, Dufour H, Chinot O, Mathon B, et al. Repeated blood–brain barrier opening with a nine-emitter implantable ultrasound device in combination with carboplatin in recurrent glioblastoma: a phase I/II clinical trial. *Nature Communications.* 2024;15(1):1650.
26. Arrieta VA, Gould A, Kim KS, Habashy KJ, Dmello C, Vázquez-Cervantes GI, et al. Enhanced delivery of doxorubicin to the brain by ultrasound induces an IFN-g phenotype of microglia, macrophages, and T cells in human glioblastoma, and improves the efficacy of PD-1 blockade in murine gliomas. *Nature Communications.* 2024;In press.
27. Hosford PS, Mosienko V, Kishi K, Jurisic G, Seuwen K, Kinzel B, et al. CNS distribution, signalling properties and central effects of G-protein coupled receptor 4. *Neuropharmacology.* 2018;138:381-92.
28. Yang LV, Radu CG, Roy M, Lee S, McLaughlin J, Teitell MA, et al. Vascular abnormalities in mice deficient for the G protein-coupled receptor GPR4 that functions as a pH sensor. *Mol Cell Biol.* 2007;27(4):1334-47.

29. Dehouck B, Fenart L, Dehouck MP, Pierce A, Torpier G, and Cecchelli R. A new function for the LDL receptor: transcytosis of LDL across the blood-brain barrier. *J Cell Biol.* 1997;138(4):877-89.
30. Molino Y, David M, Varini K, Jabes F, Gaudin N, Fortoul A, et al. Use of LDL receptor-targeting peptide vectors for in vitro and in vivo cargo transport across the blood-brain barrier. *FASEB J.* 2017;31(5):1807-27.
31. Zaragozá R. Transport of Amino Acids Across the Blood-Brain Barrier. *Front Physiol.* 2020;11:973.
32. Lee WJ, Hawkins RA, Viña JR, and Peterson DR. Glutamine transport by the blood-brain barrier: a possible mechanism for nitrogen removal. *Am J Physiol.* 1998;274(4):C1101-7.
33. Dolgodilina E, Imobersteg S, Laczko E, Welt T, Verrey F, and Makrides V. Brain interstitial fluid glutamine homeostasis is controlled by blood-brain barrier SLC7A5/LAT1 amino acid transporter. *J Cereb Blood Flow Metab.* 2016;36(11):1929-41.
34. Mokgokong R, Wang S, Taylor CJ, Barrand MA, and Hladky SB. Ion transporters in brain endothelial cells that contribute to formation of brain interstitial fluid. *Pflugers Arch.* 2014;466(5):887-901.
35. Geier EG, Chen EC, Webb A, Papp AC, Yee SW, Sadee W, et al. Profiling solute carrier transporters in the human blood-brain barrier. *Clin Pharmacol Ther.* 2013;94(6):636-9.
36. Schäfer AM, Meyer Zu Schwabedissen HE, and Grube M. Expression and Function of Organic Anion Transporting Polypeptides in the Human Brain: Physiological and Pharmacological Implications. *Pharmaceutics.* 2021;13(6).
37. Song HW, Foreman KL, Gastfriend BD, Kuo JS, Palecek SP, and Shusta EV. Transcriptomic comparison of human and mouse brain microvessels. *Scientific Reports.* 2020;10(1):12358.
38. Sheikov N, McDannold N, Vykhodtseva N, Jolesz FA, and Hynynen K. Cellular Mechanisms of the Blood-Brain Barrier Opening Induced By Ultrasound In Presence of Microbubbles. *Ultrasound in Med & Biol.* 2004;30(7):979-89.
39. Sheikov N, McDannold N, Jolesz F, Zhang YZ, Tam K, and Hynynen K. Brain arterioles show more active vesicular transport of blood-borne tracer molecules than capillaries and venules after focused ultrasound-evoked opening of the blood-brain barrier. *Ultrasound Med Biol.* 2006;32(9):1399-409.
40. Jeanne M, Jorgensen J, and Gould DB. Molecular and Genetic Analyses of Collagen Type IV Mutant Mouse Models of Spontaneous Intracerebral Hemorrhage Identify Mechanisms for Stroke Prevention. *Circulation.* 2015;131(18):1555-65.
41. Xu L, Nirwane A, and Yao Y. Basement membrane and blood-brain barrier. *Stroke Vasc Neurol.* 2019;4(2):78-82.
42. Li W, Chen Z, Chin I, Chen Z, and Dai H. The Role of VE-cadherin in Blood-brain Barrier Integrity Under Central Nervous System Pathological Conditions. *Curr Neuropharmacol.* 2018;16(9):1375-84.
43. Citi S, Pulimeno P, and Paschoud S. Cingulin, paracingulin, and PLEKHA7: signaling and cytoskeletal adaptors at the apical junctional complex. *Ann N Y Acad Sci.* 2012;1257:125-32.

44. Tornavaca O, Chia M, Dufton N, Almagro LO, Conway DE, Randi AM, et al. ZO-1 controls endothelial adherens junctions, cell-cell tension, angiogenesis, and barrier formation. *J Cell Biol.* 2015;208(6):821-38.
45. Shi Y, Zhang L, Pu H, Mao L, Hu X, Jiang X, et al. Rapid endothelial cytoskeletal reorganization enables early blood-brain barrier disruption and long-term ischaemic reperfusion brain injury. *Nat Commun.* 2016;7:10523.
46. Yang YR, Xiong XY, Liu J, Wu LR, Zhong Q, Zhou K, et al. Mfsd2a (Major Facilitator Superfamily Domain Containing 2a) Attenuates Intracerebral Hemorrhage-Induced Blood-Brain Barrier Disruption by Inhibiting Vesicular Transcytosis. *J Am Heart Assoc.* 2017;6(7).
47. Zhao C, Ma J, Wang Z, Li H, Shen H, Li X, et al. Mfsd2a Attenuates Blood-Brain Barrier Disruption After Sub-arachnoid Hemorrhage by Inhibiting Caveolae-Mediated Transcellular Transport in Rats. *Transl Stroke Res.* 2020;11(5):1012-27.
48. Eze UC, Bhaduri A, Haeussler M, Nowakowski TJ, and Kriegstein AR. Single-cell atlas of early human brain development highlights heterogeneity of human neuroepithelial cells and early radial glia. *Nat Neurosci.* 2021;24(4):584-94.
49. Vanlandewijck M, He L, Mäe MA, Andrae J, Ando K, Del Gaudio F, et al. A molecular atlas of cell types and zonation in the brain vasculature. *Nature.* 2018;554(7693):475-80.
50. Winkler EA, Kim CN, Ross JM, Garcia JH, Gil E, Oh I, et al. A single-cell atlas of the normal and malformed human brain vasculature. *Science.* 2022;375(6584):eabi7377.
51. Hynynen K, McDannold N, Sheikov NA, Jolesz FA, and Vykhodtseva N. Local and reversible blood-brain barrier disruption by noninvasive focused ultrasound at frequencies suitable for trans-skull sonications. *Neuroimage.* 2005;24(1):12-20.
52. Przystupski D, and Ussowicz M. Landscape of Cellular Bioeffects Triggered by Ultrasound-Induced Sonoporation. *Int J Mol Sci.* 2022;23(19).
53. Sinha B, Koster D, Ruez R, Gonnord P, Bastiani M, Abankwa D, et al. Cells respond to mechanical stress by rapid disassembly of caveolae. *Cell.* 2011;144(3):402-13.
54. del Pozo MA, Balasubramanian N, Alderson NB, Kiosses WB, Grande-Garcia A, Anderson RG, et al. Phospho-caveolin-1 mediates integrin-regulated membrane domain internalization. *Nat Cell Biol.* 2005;7(9):901-8.
55. Chu PC, Chai WY, Tsai CH, Kang ST, Yeh CK, and Liu HL. Focused Ultrasound-Induced Blood-Brain Barrier Opening: Association with Mechanical Index and Cavitation Index Analyzed by Dynamic Contrast-Enhanced Magnetic-Resonance Imaging. *Sci Rep.* 2016;6:33264.
56. Idbaih A, Canney M, Belin L, Desseaux C, Vignot A, Bouchoux G, et al. Safety and Feasibility of Repeated and Transient Blood-Brain Barrier Disruption by Pulsed Ultrasound in Patients with Recurrent Glioblastoma. *Clin Cancer Res.* 2019;25(13):3793-801.
57. O'Reilly MA, Hough O, and Hynynen K. Blood-Brain Barrier Closure Time After Controlled Ultrasound-Induced Opening Is Independent of Opening Volume. *J Ultrasound Med.* 2017;36(3):475-83.
58. Satija R, Farrell JA, Gennert D, Schier AF, and Regev A. Spatial reconstruction of single-cell gene expression data. *Nat Biotechnol.* 2015;33(5):495-502.

59. McGinnis CS, Murrow LM, and Gartner ZJ. DoubletFinder: Doublet Detection in Single-Cell RNA Sequencing Data Using Artificial Nearest Neighbors. *Cell Syst.* 2019;8(4):329-37.e4.
60. Korsunsky I, Millard N, Fan J, Slowikowski K, Zhang F, Wei K, et al. Fast, sensitive and accurate integration of single-cell data with Harmony. *Nat Methods.* 2019;16(12):1289-96.
61. Franzen O, Gan LM, and Bjorkegren JLM. PanglaoDB: a web server for exploration of mouse and human single-cell RNA sequencing data. *Database (Oxford).* 2019;2019.
62. Corces MR, Shcherbina A, Kundu S, Gloudemans MJ, Fresard L, Granja JM, et al. Single-cell epigenomic analyses implicate candidate causal variants at inherited risk loci for Alzheimer's and Parkinson's diseases. *Nat Genet.* 2020;52(11):1158-68.
63. Preissl S, Fang R, Huang H, Zhao Y, Raviram R, Gorkin DU, et al. Single-nucleus analysis of accessible chromatin in developing mouse forebrain reveals cell-type-specific transcriptional regulation. *Nat Neurosci.* 2018;21(3):432-9.
64. Welch JD, Kozareva V, Ferreira A, Vanderburg C, Martin C, and Macosko EZ. Single-Cell Multi-omic Integration Compares and Contrasts Features of Brain Cell Identity. *Cell.* 2019;177(7):1873-87.e17.
65. Zhu C, Zhang Y, Li YE, Lucero J, Behrens MM, and Ren B. Joint profiling of histone modifications and transcriptome in single cells from mouse brain. *Nat Methods.* 2021;18(3):283-92.
66. Yu G, Wang LG, Han Y, and He QY. clusterProfiler: an R package for comparing biological themes among gene clusters. *OMICS.* 2012;16(5):284-7.

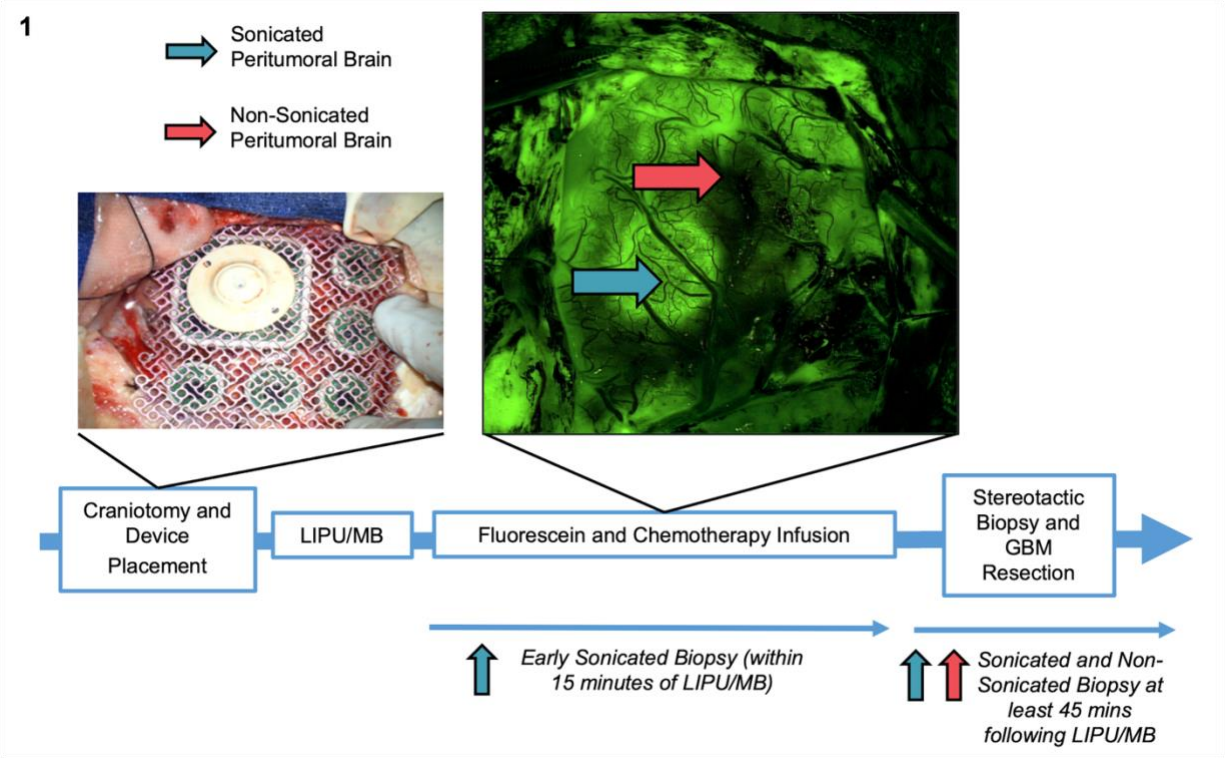

Figure 1. Schematic of intraoperative LIPU/MB procedure and time course of peri-tumoral brain biopsy. Photo from surgical microscope shows hyperfluorescent areas of dysfunctional BBB shortly after LIPU/MB and infusion of chemotherapy with fluorescein bolus as previously described (24). Blue arrows indicate sonicated peri-tumoral brain and pink arrows indicate non-sonicated peri-tumoral brain. Sonicated peri-tumoral brain biopsies were collected at "early" timepoints after LIPU/MB (within 15 minutes) and at later timepoints (at least 45 minutes after LIPU/MB).

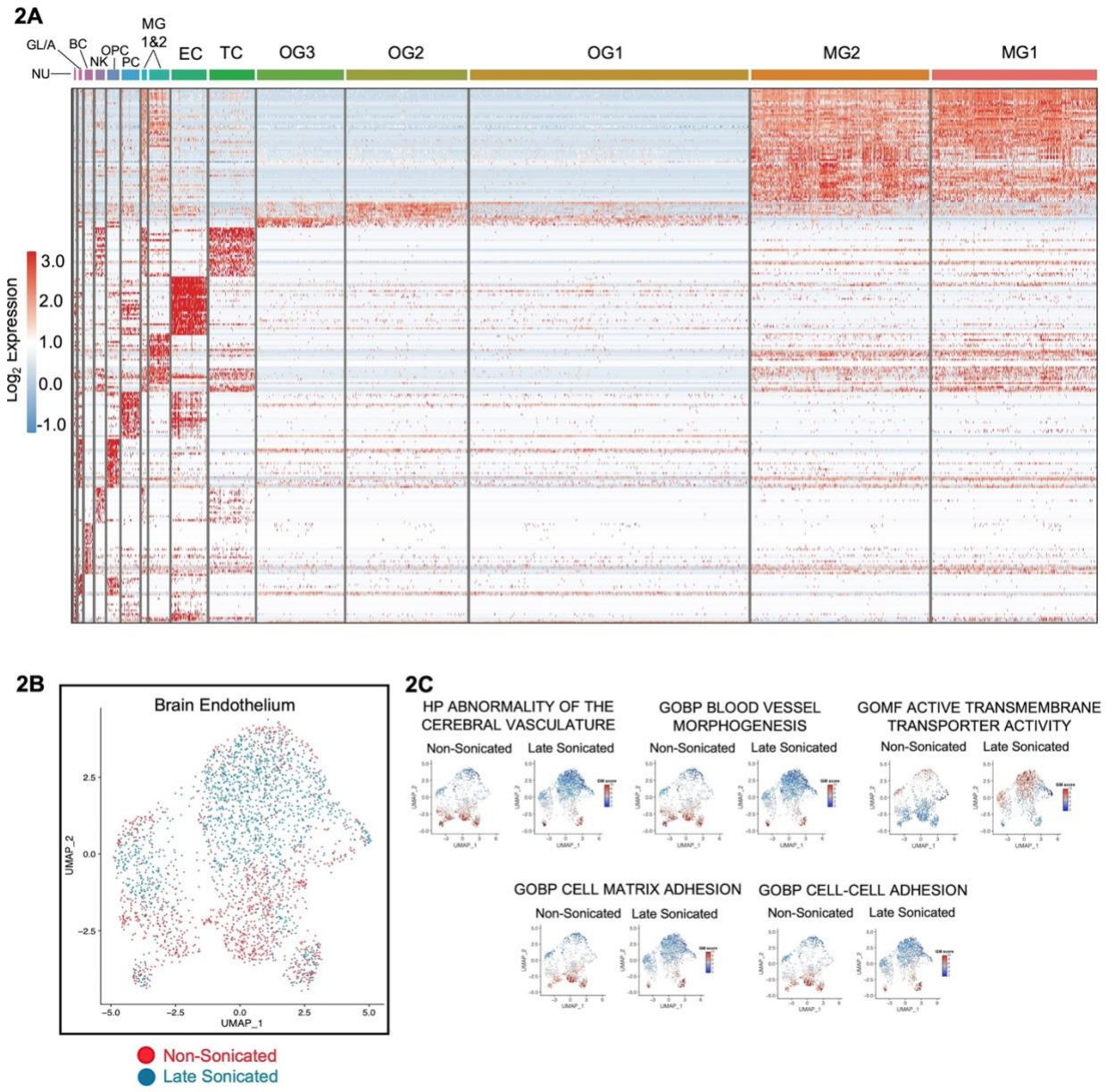

Figure 2. LIPU/MB-mediated BBB disruption alters the transcriptional phenotype of cerebral endothelial cells. The single-cell transcriptional analysis derived from 6 patients with paired sonicated and non-sonicated peri-tumoral brain samples. Total of 2643 ECs, including 1470 from sonicated and 1173 derived from non-sonicated peri-tumoral brain specimens collected approximately 45 minutes after LIPU/MB (**A).** Heatmap illustrates the identity of 14 separate clusters of cells derived from the peri-tumoral brain, including endothelial cells, isolated from sonicated and non-sonicated peritumoral brain tissues. Corresponding names for each cell type are listed along the left side of the heatmap (MG1: Type 1 Microglia; MG2: Type 2 Microglia; OG1: Oligodendrocyte 1; OG2: Oligodendrocyte 2; OG3: Oligodendrocyte 3; TC: T-Cells; EC: Endothelial Cells; MC 1&2: Monocytes 1 and 2; PC: Pericytes; OPC: Oligodendrocyte Progenitor Cell; NK: Natural Killer Cell; BC: B-Cell; GL/A: Glioma Cells and Astrocytes; NU: Neurons). (**B)**

Representative UMAP cluster showing gene expression profiles for ECs with sonicated subpopulation in blue and non-sonicated in red. (**C)** UMAP plots illustrate gene expression changes related to select GO themes that had significant differences between non-sonicated control and sonicated ECs (GSEA adjusted $p<0.05$).

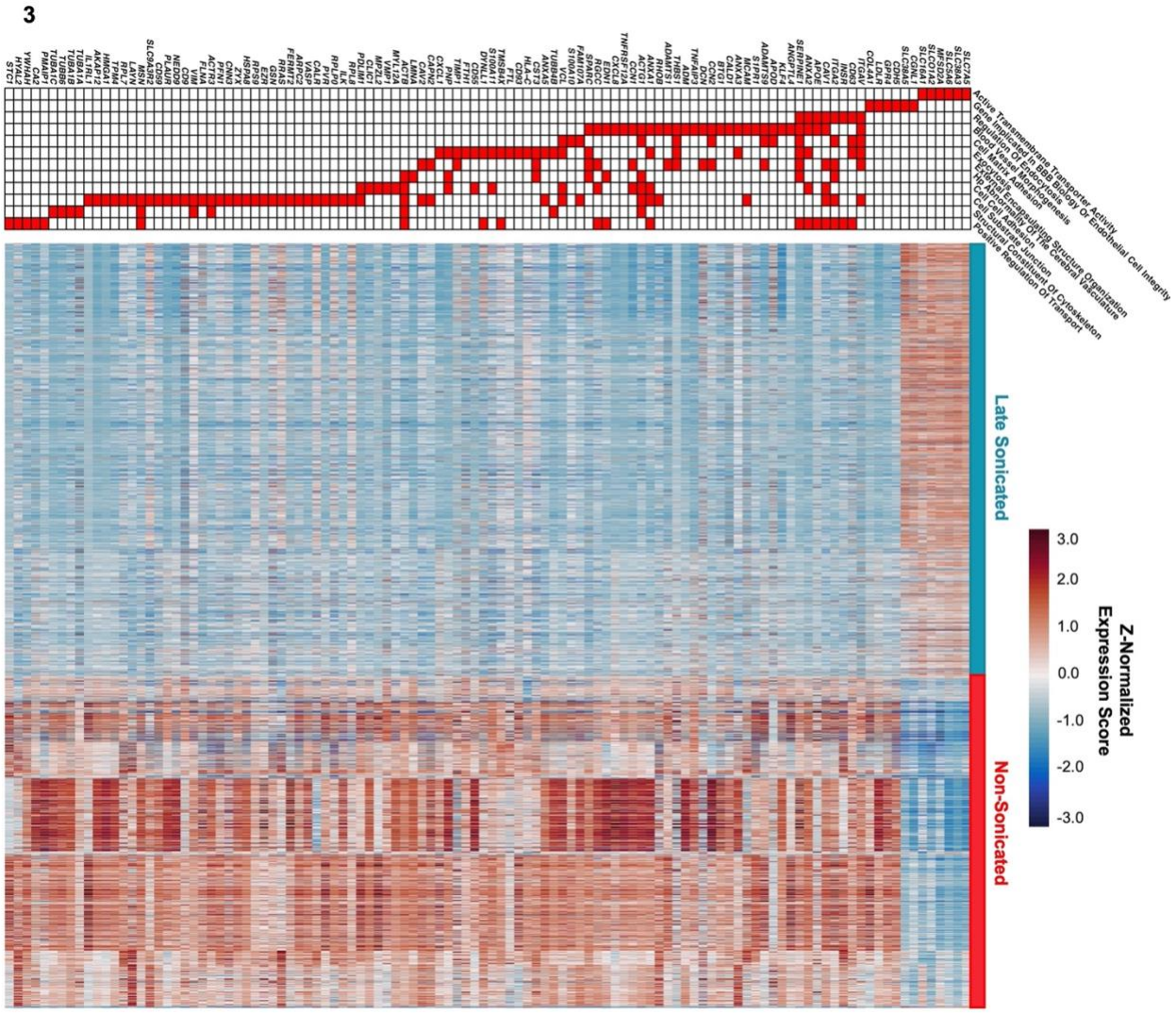

Figure 3. Gene expression changes in cerebral endothelial cells following LIPU/MB-mediated BBB disruption. Derived from 6 patients with paired sonicated and non-sonicated peri-tumoral brain samples Heatmap illustrates Z-score normalized expression changes of individual genes altered between sonicated and control ECs from the GO themes described in figure 2, as well as individual genes that have been implicated in BBB biology or EC homeostasis. The top of heatmap diagram shows the involvement of individual genes on each of these GO themes.

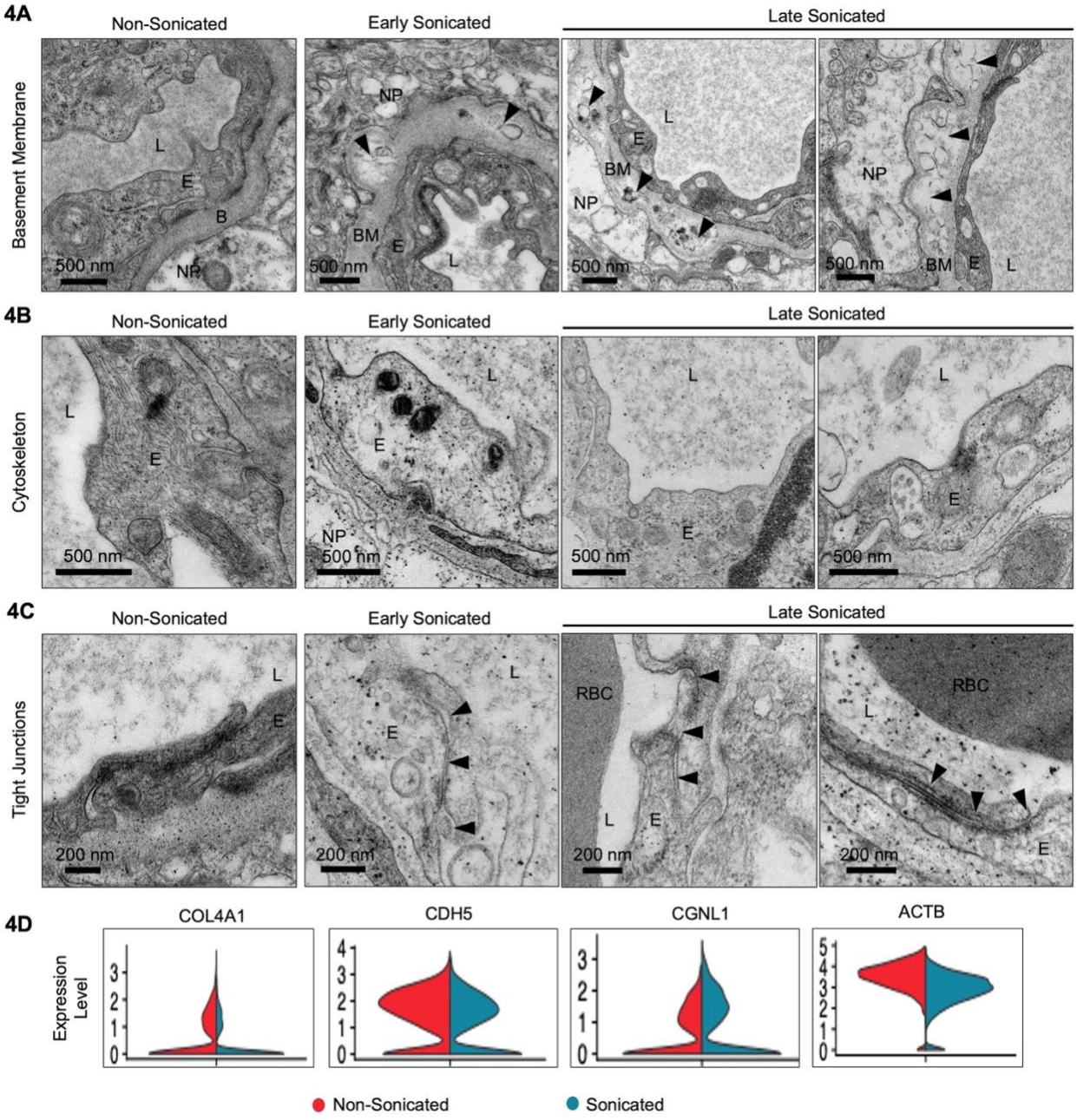

Figure 4. Ultrastructural alterations to brain capillaries following LIPU/MB- -Mediated BBB Disruption. Representative electron micrographs highlighting various structural abnormalities observed in the cerebral capillaries of peritumoral tissues after sonication. Representative transmission electron micrographs with scale bars show highlighted features from capillary cross sections acquired from non-sonicated peri-tumoral brain tissue, sonicated brain tissue early after LIPU/MB (4-15 minutes), and sonicated brain tissues late after LIPU/MB (57-63 minutes). Paired brain tissue samples from each time point were acquired from 3 separate patients, for a total of 9 tissue biopsies. Accompanying scale bars are used throughout and relevant features of the capillary structure are denoted by the following letters: L (Vascular Lumen), E (Endothelial

Cytoplasm), B (Basement Membrane), NP (Neuropil). **(A).** Sonicated capillaries frequently demonstrated irregular granular deposits or focal areas of amorphous enlargement, highlighted by arrowheads **(B).** Within sonicated capillaries we also observed rarefaction of the endothelial cytosol and cytoskeletal disorganization **(C).** We occasionally observed that TJ complexes appeared less dense than in their non-sonicated counterparts, with evidence of opening and irregular spacing between adjoining surfaces of the EC, with irregularities are denoted by arrowheads **(D).** Representative violin plots for normalized expression changes of genes that code for proteins associated with either basement membrane (*COL4A1*), cytoskeleton (*ACTB*), or the TJ complex (*CDH5, CGNL1*) in sonicated and non-sonicated tissues.

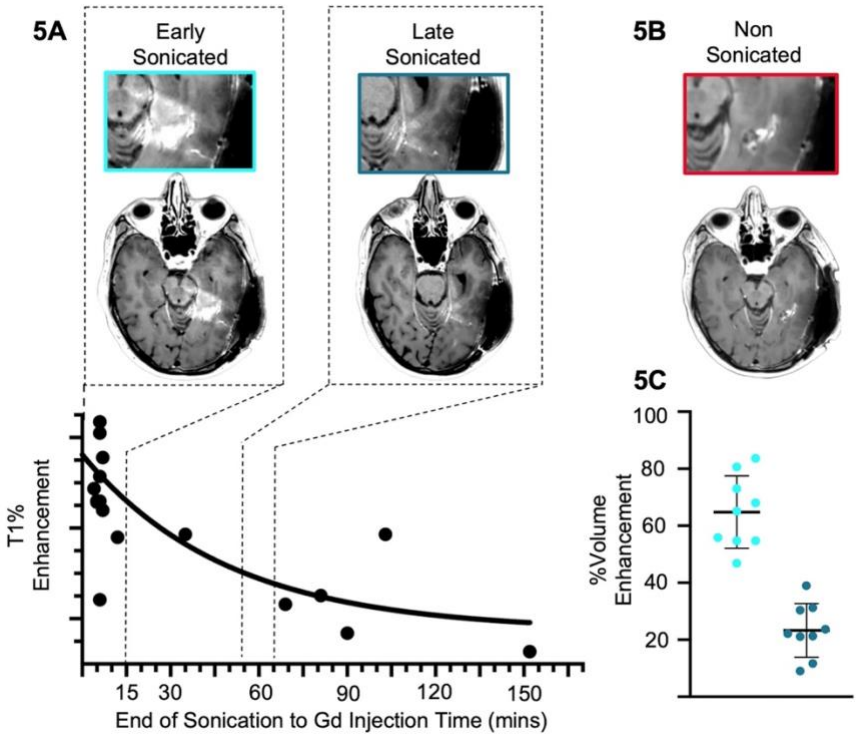

Figure 5. Radiographic estimate BBB closure kinetics following acute disruption by LIPU/MB. (A). BBB permeability analysis from 17 patients, derived from post-LIPU/MB enhancement on MRI where variable time between LIPU/MB and gadolinium injection is shown on the X-axis and % of T1 enhancement is on the Y-axis (derived from data reported previously (24)). Curve represents a linear mixed-effects regression model (β = -0.2839, 95% C.I. -0.4254, -0.1424, p = 0.00056) as we previously reported (24)**.** Above are corresponding T1 Post Contrast MRI from a representative patient, showing the relative permeability of the BBB at the timepoint of gadolinium administration following LIPU/MB. The highlight outlined in light blue represents the relative permeability of the BBB shortly after sonication (within 15 minutes) and MRI highlighted in dark blue corresponds to permeability at least 45 minutes after LIPU/MB. Dotted lines drawn down from these highlights correspond to the timepoints of tissue acquisition presented on the X-axis **(B).** T1 Post Contrast MRI, highlighted in red, from the same patient before sonication demonstrate the relative impermeability of non-sonicated brain **(C).** Dot plots show change in %volume of enhancement in peritumoral brain targeted by ultrasound emitters from the SC9 device (n = 9 regions of peritumoral brain) when compared to baseline non-sonicated MRI in early sonicated (light blue) and late sonicated (darker blue). Data are the mean ± SD. Figure generated from data previously reported on Sonabend et al., Lancet Oncology 2023 (24).

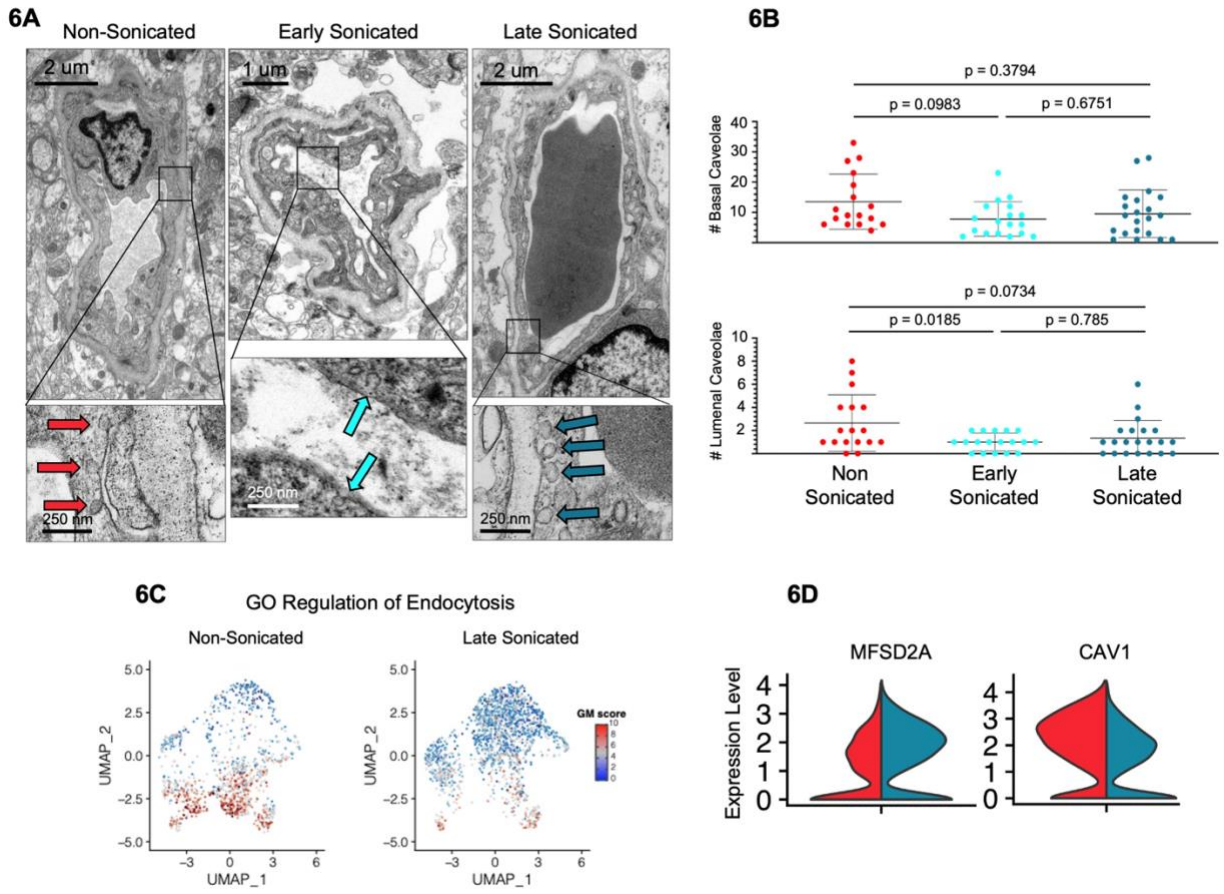

Figure 6. Ultrasound-Mediated BBB Disruption Alters Cerebral Endothelial Caveolar Pit Density in a Time-Dependent Fashion. (A). Representative TEM micrographs with scale bars show capillary cross sections acquired from non-sonicated, early sonicated, and late sonicated peri-tumoral brain tissue. Permeability of the BBB at the timepoints of acquisition can be estimated by the radiographs in 5A. Magnifications in the lower panels show caveolar pits attached to the basement and luminal membranes of the endothelium. Paired brain tissue samples from each time point were acquired from 3 separate patients, for a total of 9 tissue biopsies. Caveolae from early sonicated brain are highlighted by light blue arrows, late sonicated by darker blue, and non-sonicated by red. **(B).** Dot plots depict the total number of endothelial caveolae counted across all capillary cross sections at each timepoint (N for each group as follows: non-sonicated = 17, early sonicated = 18, late sonicated = 21), with colors matching the timepoints previously mentioned. Data are the mean ± SD. A mixed effects model was constructed considering 'sonication' as a fixed effect and 'patient' as a random effect influencing the number of caveolae. P values displayed on this panel are from a post-hoc analysis and were obtained by likelihood ratio tests of the full model with the effect in question against the model without the effect in question. (**C).** UMAP plots demonstrate relative expression of genes pertinent to GO Theme Regulation of Endocytosis within non-sonicated and late sonicated ECs. Legend for GM score on rightmost side. (**D).** Representative violin plots for normalized expression of genes *MFSD2A* and *CAV1* in both non-sonicated and sonicated ECs from peri-tumoral brain tissues.

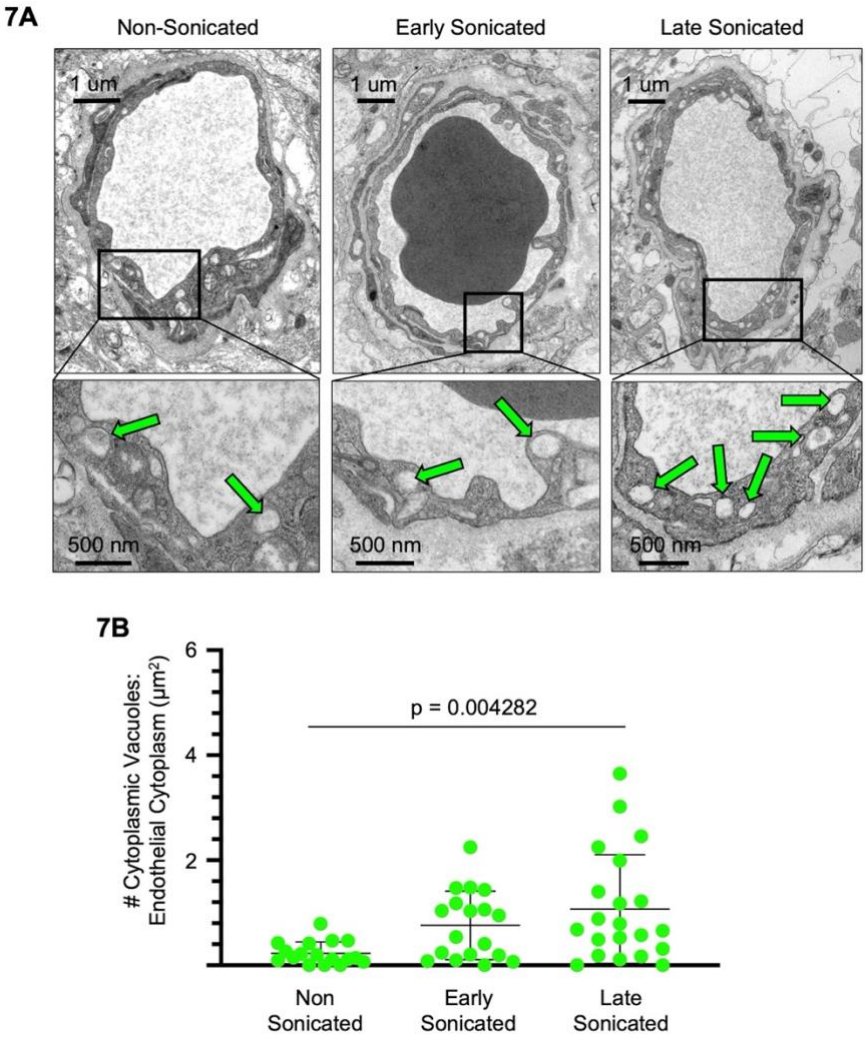

Figure 7. LIPU/MB-Mediated BBB Disruption Increases Endothelial Cytoplasmic Vacuoles Over Time. (A). Representative transmission electron micrographs with scale bars show capillary cross sections acquired from non-sonicated peri-tumoral brain tissue, sonicated brain tissue early after LIPU/MB (4-15 minutes), and sonicated brain tissues late after LIPU/MB (57-63 minutes). Paired brain tissue samples from each time point were acquired from 3 separate patients, for a total of 9 tissue biopsies Magnifications in the lower panels show vacuoles within the endothelial cytoplasm, highlighted by green arrows. **(B).** Dot plots depicting the number of endothelial cytoplasmic vacuoles normalized to the total cross-sectional surface area of the total endothelial cytoplasm for each capillary (N for each group as follows: non-sonicated = 17, early sonicated = 18, late sonicated = 21). Data are the mean ± SD. P value is derived from a mixed effects model, constructed under the consideration of 'sonication' as a fixed effect and 'patient' as a random effect influencing the number of normalized vacuoles.

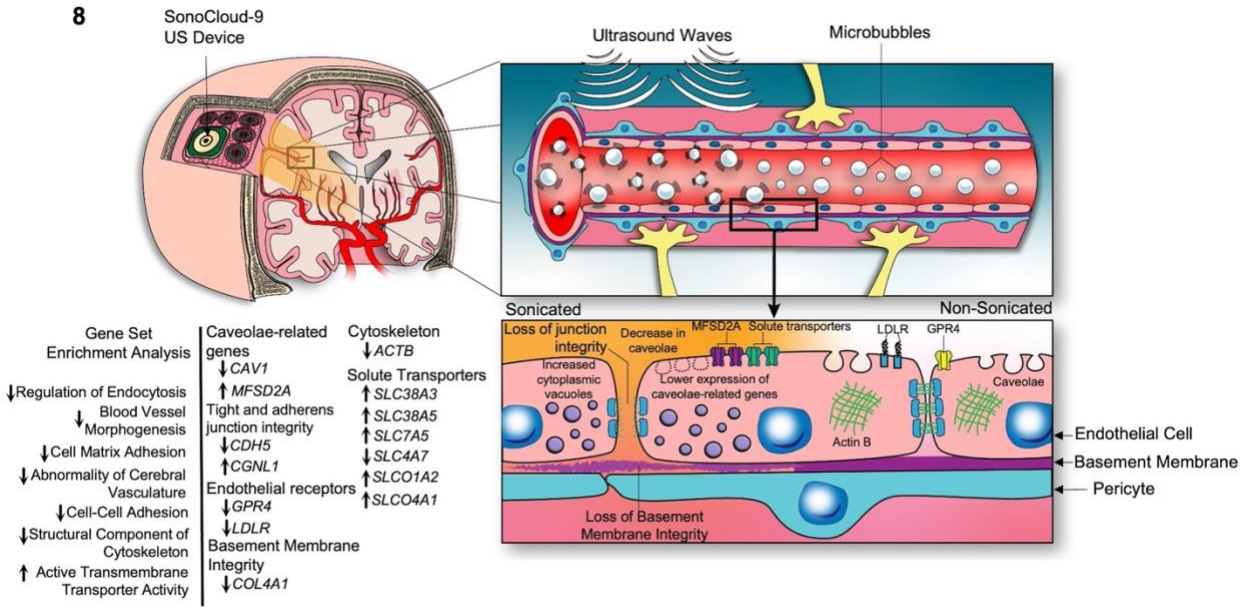

Figure 8. Illustration of Transcriptional and Structural Consequences of Ultrasound-Mediated BBB Disruption on the Cerebral Endothelium. Cartoon summarizing the key transcriptional and ultrastructural changes to the cerebral ECs that were observed following sonication.